A comparative study of some kaolinites surface properties

J.A. Mbey, F. Thomas, A. Razafitianamaharavo, C. Caillet, F. Villiéras

A comparative study of some kaolinites surface properties

J.A. Mbey [1, 2*], F. Thomas [2, 3], A. Razafitianamaharavo [2, 3],
C. Caillet [2], and F. Villieras [2, 3]

[1] *University of Yaounde I, Department of Inorganic Chemistry, P.O. BOX 812 Yaoundé*

[2] *Université de Lorraine, Laboratoire Interdisciplinaire des Environnements Continentaux, UMR 7360, 15 Avenue du Charmois, B.P. 40. F-54501, Vandœuvre-lès-Nancy Cedex*

[3] *CNRS, Laboratoire Interdisciplinaire des Environnements Continentaux, UMR 7360, 15 Avenue du Charmois, B.P. 40. F-54501, Vandœuvre-lès-Nancy Cedex*

[*]e-mail: mbey25@yahoo.fr ; jambey@uy1.uninet.cm

ABSTRACT: The surface properties of five kaolinites of various origins were analyzed using potentiometric titration, electrokinetic measurements and low-pressure gas adsorption associated to derivative isotherm summation (DIS) modeling. The data show that sample structure is important in determining the surface properties. The combined analytical results clearly shows the existence of a permanent negative layer charge for all the samples. The general features that could be observed for the five kaolinites are: the titration curves are shifted to lower pH with increasing ionic strength due to the layer charge; the amount of consumed proton is influenced by the permanent layer charge; although low, the permanent charge determines the electrokinetic behavior. The shape anisotropy and the charge distribution on the basal and edge surfaces are crucial parameters to understand the behavior of kaolinite particles in aqueous media. The Cameroonian sample of the set exhibits a significant permanent charge together with large specific surface area associated to fine particle size and considerable shape anisotropy.

Keywords: Kaolinite; Electrokinetic; Potentiometric titration; Surface; DIS Modeling

1. INTRODUCTION

Clays are raw materials of importance in various domains such as agriculture, material engineering, health and environmental issues. Amongst clays, kaolin occurrences are common. Primary kaolin deposits are of hydrothermal or residual origin (or mixed hydrothermal and residual); secondary deposits are sedimentary (Murray, 2000; Bergaya et al., 2006; Menezes et al., 2017). The most common clay mineral within the kaolin group is kaolinite (kaol). Each kaol layer is formed by the superposition of one aluminium hydroxide octahedral sheet and one silica tetrahedral sheet. Thus, a kaol layer has asymmetrical basal planes: siloxane and hydroxylated alumina. Basal planes of kaol carry a small permanent negative charge due to isomorphous substitution in both octahedral and tetrahedral sheets, whereas the edge surfaces carry a pH-dependant variable charge due to the protonation/deprotonation of edge hydroxyl groups from broken bonds (Schofield and Samson, 1954; Williams and Williams, 1978; Bolland et al., 1980; Herrington and al., 1992). However, as far as the permanent charge is concerned, cation substitutions in the lattice of kaol are scarce, and the resulting small deviations from stoichiometry are difficult to detect by direct chemical analysis. However, even a small surface charge may influence the surface properties of kaol. In addition, the anisotropic and platy structure of kaol layers also influences its surface properties. Ma and Eggleton (1999b) have shown, using high-resolution transmission electron microscopy, that three types of surface layers may exist on a natural kaol crystal. Type 1 has the expected 0.7 nm surface layer as termination. Type 2 has one 1 nm pyrophyllite-like (or low beidellite-like) layer as the surface layer on one side of a kaol particle (ie. TOTOTO…TOTOT, where T and O stand respectively for the tetrahedral and the octahedral sheet). The spacing between the TOT (1 nm thick) and the TO (0.7 nm thick) is non-expandable due to hydrogen bonds. Type 3 has one or several 1 nm collapsed smectite-like layers at one or both side of a stack forming a special kind of kaol-smectite

50 interstratification. The latter type was observed by these authors only on some poorly ordered
51 kaol.
52 Primarily, the kaol surface charge was investigated through cation exchange capacity (CEC)
53 and potentiometric titration. Ma and Eggleton (1999a), show that the CEC is mainly due to
54 the edges and to basal hydroxyl surface of the mineral. They also conclude that permanent
55 negative charge due to isomorphous substitution is significant. Angove and al., (1997),
56 studied the adsorption of cadmium on kaol. They were able to fit the adsorption data to a
57 simple Langmuir model at pH 5.5. However at pH 7.5, a better fit was obtained with a two-
58 site Langmuir model. In the same work, titration experiments allowed for a close fit by a
59 constant capacitance surface complex model that incorporates two bidentate surface
60 complexes. The results from their experiments were consistent with the view that Cd(II)
61 adsorbs to kaol by two distinct processes : ion-exchange at the permanently charged sites on
62 the silanol face and surface complexation to aluminol and silanol groups occurring at the
63 crystal edges. In a comparative study of transition metals adsorption on kaol, Ikhasan et al.,
64 (1999) came to the same conclusion. Zhou and Gunter (1992), examined the kaol surface
65 charge in the light of surface charge density and showed, through kaol CEC variation with
66 pH, that the ionization of the basal surface also takes place in aqueous solution. Nevertheless,
67 this contribution of basal faces seems not to be significant enough according to Brady and al.,
68 (1996), who explain pH-dependent surface charges in kaol by proton donor–acceptor
69 reactions. Based on the measured proton adsorption isotherms and molecular modeling of
70 proton-relaxed kaol structure, the authors show that edge sites contribute more to kaol charge
71 development, and point out that edge surfaces represent 10 to 50% of the total area, showing
72 that usual estimation of 20% maximum could be an underestimation. Huertas et al., (1998)
73 used a multi-site model to compute the surface properties of kaol and reported that the surface
74 charge of kaol in an inert electrolyte solution involves three different surface sites: external

hydroxo-aluminium in the octahedral layer, weak Al acidic site, and silanol groups at the crystal edges. Protonation-deprotonation of these groups depending on the pH determines the surface charge.

In recent years, potentiometric titration and electrokinetic measurement techniques were commonly used to explore the surface charge of clay minerals (Schroth and Sposito, 1997; Thomas et al., 2002; Appel et al., 2003; Avena et al., 2003; Duc et al., 2006; Tertre et al., 2006; Tombácz and Szekeres, 2006; Chassagne et al., 2009; Zhu et al., 2016). Kraepiel et al. (1998) described the acid-base behavior of permanently charged minerals by applying a surface complexation model to montmorillonite and kaol. For kaol, protonation-deprotonation reactions were supposed to take place both on the edges (Al-OH groups) and on the gibbsite basal planes (Al-O-Al groups). The above authors quoted that kaol does not correspond exactly to the model solid, given that the permanent and variable charge distributions are not uniform on the clay surface. In addition, two different surfaces, basal planes and edges, are involved in the acid-base chemistry of clay, which is far from a representation of the interface as an infinite plane. The evaluation of the dissociable charge is still challenging as reported by Duc et al., (2005a). These authors reported, in their review, that the discrepancies amongst the titration data in the literature are due to the experimental procedures for the preparation of the clays and for the quantification of the charge. In two subsequent experimental papers, the same authors found evidences for the origin of this dependency and arouse some critical points for the best experimental conditions: wet storage of the clay, inert gas atmosphere for titration to avoid carbonation, and short interval time between successive titrant increments to minimize side reactions. They also established that continuous titration is more reliable than batch titration for quantifying the surface charge of clays (Duc et al., 2005b, 2006).

The discrepancies of surface charge data of clays are also due to the anisotropic nature of the platelets, and to the non-uniform distribution of their surface charge on the basal and edge

faces. Electrokinetic studies mostly deal with the measurements of the electrophoretic mobility. For kaol, many studies can be found (Williams and Williams, 1978; Rowlands and O'brien, 1995; Kosmulski and Dahlsten, 2006; Tombácz and Szekeres, 2006; Chassagne et al., 2009; Zhu et al., 2016). Many of these studies are consistent with each other, but there is a great variability for the positioning of the iso-electric point (IEP), which is the pH of zero mobility. As pointed out by some authors, this variability can be attributed to differences in chemical composition of the studied samples, to the preparation of the samples, and their history (Tombácz and Szekeres, 2006; Chassagne et al., 2009).

Low pressure gas adsorption investigations based on the Derivative Isotherm Summation (DIS) method described by Villiéras et al., (1992) is a versatile tool to quantify the surface heterogeneity distribution of minerals, and especially on kaol. Also the clay particles anisotropy can be accessed through DIS. A correlation between the edge surface area from DIS and the experimental CEC makes it possible to establish the origin of the CEC and to conclude on the existence of isomorphous substitution and presence of minor amounts of smectite (Cases et al., 2000; Villieras et al., 2002; Sayed Hassan et al., 2005). More recently, atomic force microscopy (AFM) was used by Gupta and Miller (2010) to specifically characterize the alumina and the silica layer of the kaol sheet.

The purpose of the present study was to investigate the effect of very low layer substitution in kaol on their surface charge properties in aqueous salt solution. Therefore, four "reference" samples were selected for their different origins, and for their low (but not zero) amount of crystal layer substitutions. A sample from Cameroon was included in the study, since it already showed interesting ability for industrial applications, and more precisely as reinforcing phase in composite materials made of cassava starch (Mbey et al., 2012, 2015; Mbey and Thomas, 2015). A consistent analysis of the surface properties of the Mayouom sample may be useful to impulse or ameliorate its potential use in composites making.

125 The five samples underwent a broad set of analyses in order to draw an extensive picture of
126 their crystallo-chemical, textural and surface properties at the solid-gas and solid-electrolyte
127 interface. From the literature investigation carry out for this work, no similar work was found.
128 More particularly, the use of the DIS method for such comparative study is a premiere.

129 **2. MATERIALS AND METHODS**

130 ***2.1. Kaol samples* sources and Na-kaol preparation**

131 The sources of the five studied samples are given in table I. The samples were collected
132 through wet sieving over a 40 µm mesh. The cakes obtained after sedimentation were dried in
133 an oven for 24 hours at 70°C prior to use. The particle size distribution of the collected
134 fractions was analysed using a Sympatec laser diffraction granulometer equipped with the
135 HELOS optical system and the WINDOX software for data collection.

136 Sodium exchanged samples (Na-kaol) were prepared by two successive exchanges of 5 g of
137 kaol in 125 mL of 1 M NaCl solution. For the first exchange, the clay sample was stirred in 1
138 M NaCl solution for two hours and the dispersion was centrifuged at 9000 rpm during 10 min.
139 The kaol cake was further dispersed in 1 M NaCl solution and stirred overnight. The clay cake
140 recovered by centrifugation then underwent four washing cycles in deionised water for
141 chloride and excess cations elimination, by alternating dispersion in water and centrifugation
142 at 9000 rpm during 10 min. The elimination of chloride ions from the supernatant was tested
143 using a 0.1 M solution of $AgNO_3$. The final clay cake was oven dried at 50°C during 24 hours
144 and stored in polyethylene bottle prior to subsequent use.

145 ***2.2. Chemical analysis***

146 Chemical analysis for major elements was obtained by inductive coupled plasma by atomic
147 emission spectrometry (ICP-AES) at the *Service d'Analyse des Roches et des Minéraux*
148 (SARM, Nancy, France). The samples were fused in lithium metaborate ($LiBO_2$) and
149 dissolved in nitric acid prior to analysis.

2.3. X-ray diffraction

Powder X-Ray diffraction patterns on bulk samples were recorded using a D8 Advance Bruker diffractometer equipped with a Co Kα radiation (λ = 1.7890 Å) operating at 35 kV and 45 mA. The diffraction patterns were obtained from 1.5° to 32° at a scanning rate of 1° min^{-1}. For the oriented clay mounts, samples are dispersed in water and left to settle for about 30 min in order to select the < 2 μm fraction in the supernatant, according to the Stokes' law. Oriented clay mounts were obtained by depositing drops of supernatant on a glass slide and drying, prior to special treatments including glycolation and firing at 550°C. The XRD patterns of the oriented and treated samples were recorded from 1º to 20º (θ).

The coherent scattering domain (*D*) was calculated from X-ray patterns using the full width at maximum half height of the d_{001} reflection and the Scherrer equation.

2.4. Fourier Transform Infrared (FTIR) Spectroscopy.

Infrared spectra were recorded in diffuse reflectance mode using a Bruker Fourier Transform Interferometer IFS 55. The spectra, recorded from 4000 cm^{-1} to 600 cm^{-1} with a resolution of 4 cm^{-1}, are obtained by accumulation of 200 scans. Potassium bromide (KBr) pellets containing ~15% of the powder clay were obtained by pressing (10 tons/cm^2) manually ground mixtures of the clay and oven dried potassium bromide.

2.5. Electron Microscopy.

Transmission electron microscopy coupled with energy dispersive X-Ray spectroscopy (TEM-EDX) was performed on a Philips CM20 microscope operating at 200 kV.

2.6. Cation exchange capacity (CEC).

The CEC was obtained by saturation of 3 g of clay with hexaaminecobalt(III) ions ($[Co(NH_3)_6]^{3+}$). The amount of hexaaminecolbalt(III) ions adsorbed by the solid phase, was obtained after evaluation of the remaining Cobalt in the supernatant through colorimetric titration at 472 nm using UV-vis spectroscopy.

2.7. Nitrogen and Argon adsorption at 77 K.

Conventional nitrogen adsorption-desorption isotherms at 77 K were recorded on a step-by-step automatic home-built set-up. Pressures were measured using 0-1000 Pa and 0-100,000 Pa Baratron-type pressure sensors provided by Edwards. The nitrogen saturation pressure was recorded in situ using an independent 0-100,000 Pa Baratron-type pressure sensor provided by Edwards. Prior to adsorption, the samples were outgassed overnight at 110°C and under a residual pressure of 0.01 Pa. Nitrogen N55 (purity > 99.9995%) used for experiments was provided by ALPHAGAZ (France). Specific surface areas (SSA) were determined from adsorption data by applying the Brunauer-Emmet-Teller (BET) equation and using 16.3 $Å^2$ for the cross sectional area of nitrogen. In the present study, the error in the determination of the SSA was estimated as +/- 1 m^2 /g.

Low-pressure argon adsorption isotherms of Argon at 77 K were recorded on a home-made automatic quasi-equilibrium volumetric set up (Villiérias et al. 1992, 1997; Bardot et al., 1998). The Na-kaol sample was outgassed overnight at 110°C under a residual pressure of 10^{-4} Pa. High purity Argon (>99.9996%) provided by ALPHAGAZ (France) was used as an adsorbate and introduced continuously through a micro leak. Pressure measurements are performed using two differential pressure gauges (Datametrics) in the 0-10 Torr and 0-1000 Torr ranges and 0.1% accuracy. The quasi equilibrium pressures are recorded as a function of time to obtain the adsorption isotherm. More than 2000 data points are collected during the adsorption of the first layer and are plotted as the first derivative of the adsorbed quantity as a function of the logarithm of the relative pressure $\ln(P/P_0)$, which corresponds to an energy scale (T). The data are analyzed using the theoretical derivative adsorption isotherm summation (DIS), described by Villiéras et al. (1992), to examine surface heterogeneity of the samples. In this method, a heterogeneous surface is assumed to be formed of patch-wise distribution of discrete energetic domains that can be considered locally homogeneous. Thus,

200 the total derivative adsorption isotherm can be simulated by the sum of local theoretical
201 derivative adsorption isotherms on each domain (equation 1).
202 $\theta_t = \sum X_i \theta_{it}$ (1)
203 where θ_t is the total adsorption isotherm; θ_{it} is the adsorption isotherms on the different
204 energetic domains of the surface; X_i is its fractional contribution to θ_{it}.
205 The experimental derivative curve is then fitted using theoretical local isotherms derived from
206 one layer and/or multilayer adsorption formalisms (BET formalism in the case of this study).
207 The total specific surface area is the sum of the monolayer capacities of the various domains,
208 taking into account the cross sectional area of Argon (13.8 Å).
209 ***2.8. Potentiometric titration.***
210 The titration was done after the method proposed by Duc et al., (2006). Typically, the proton
211 surface excess of each Na-kaol was quantified by continuous titration at 25 ± 1°C (the
212 temperature control is ensured by the use of a thermocryostat) using a Titrando 809 titration
213 device equipped with two dosing units (Dosino 800) and a combined pH electrode. The
214 system is driven automatically by the software Tiamo (version 1.2.1 light). All the
215 experiments are conducted under magnetic stirring and under an Argon flow to prevent
216 carbonation. The pH electrode is calibrated with five buffers at the beginning of each test to
217 check the nernstian response. An average of 1g of kaol is mixed with 50 mL of $NaNO_3$
218 electrolyte solution of concentration 10^{-3} M, 10^{-2} M and 10^{-1} M. At first, the pH is increased
219 from natural pH to 9 by addition of NaOH (0.1 M) aliquots, and subsequently decreased to pH
220 3 by addition of HNO_3 (0.1 M). The NaOH and HNO_3 aliquots addition is controlled by the
221 software between 10 µl and 200 µL (100 µL in the direction of increasing pH). The delay
222 between two consecutive titrant additions is set between 50 s and 600 s for both increasing
223 and decreasing pH pathways. This delay time, after which the pH value is considered as
224 stable, is controlled by the pH drift limit set at 0.5 mV/min in the decreasing direction from

pH 9 to 3. The data recorded in this range were used to calculate the surface excess curves. A slightly larger pH drift of 1 mV/min is used in the alkaline direction to reach the starting pH of 9. The pH range 3 to 9 was chosen to limit dissolution of the samples.

The actual surface excess is calculated as the difference between the amount of H^+ or OH^- consumed by the blank electrolyte and by the suspension at each titration point. A positive sign was attributed to an excess consumption in H^+ and a negative sign was attributed to an excess consumption in OH^-. The intersection point between the blank and the suspension curves is the point of zero net proton consumption (PZNPC).

2.9. Electrophoretic mobility measurement.

Electrophoretic mobility of the Na-kaol was measured by micro-electrophoresis. In this technique, a dispersion of particles is placed in a capillary cell and submitted to an electric field. The migration rate of particle due to the electric force is then measured. The measurements were done using a Zetaphoremeter V (CAD Instrumentation). The capillary cell is placed on a microscope and lighted up at 90° by a laser. The dispersion in the cell is submitted to an electric field of 80 V/cm and a CCD camera is used to capture the particle displacement in the cell. The mobility was measured in $NaNO_3$ background (10^{-3} M, 10^{-2} M and 10^{-1} M). Dilute kaol dispersions were prepared by mixing 3 mg to 8 mg of Na-kaol with 300 mL of electrolyte solution and stirred overnight. Each dispersion was sonicated for 2 min, large aggregates were left to settle (10 minutes), and the supernatant was used for measurements. The pH was adjusted by adding aliquots of 0.1 M of NaOH or HNO_3 before introducing the dispersion in the capillary cell.

3. RESULTS AND DISCUSSION

3.1. Mineralogy and chemical composition

From X-ray diffraction (figure 1), kaol is the dominant mineral in all the samples, together with small amounts of illite/muscovite and titanium oxide. The identification was confirmed

250 on the oriented samples (figure 1b), the glycolation (figure 1c) and the thermal treatment at
251 550°C (figure 1c). The reflection at 16.33 Å in the MAC sample, denoted X, was assigned to
252 a possible illite-kaol mixed layer mineral. This conclusion was drawn from glycolation (figure
253 1c), heating at 550°C (figure 1d) and DMSO intercalation (figure 1e) experiments. After
254 glycolation (figure 1c), this reflection is not shifted, which excludes the presence of isolated
255 or interstratified swelling clay sheets. After heating (Figure 1d), the previous conclusion is
256 reinforced due to the absence of the usual collapse of smectite at 10 Å. The DMSO
257 intercalation lead to the formation of characteristic reflection of DMSO-kaol intercalate at
258 11.26 Å and no supplementary mineral phase was observed. All of the previous are in line
259 with the proposed interstratification of illite-kaol at 16.90 Å on the oriented clay mount
260 (figure 1d). This kaol mixed layer is formed of kaol including very small amounts of illite (or
261 even swelling 2:1) as also proposed by Shakarov et al. (1999) in a study on kaol-illite-
262 vermiculite mixed layer. Such mixed structure is also proposed by Hong et al. (2015) with
263 d_{001} value around 13 Å. Such mixed layer are viewed as intermediates phase formed during
264 transformation of illite to smectite, vermiculite and kaol (Hong et al, 2015).
265 The infrared spectra (Figure 2) are typical of kaol. The characteristic bands at 3697, 3666,
266 3651 and 3620 cm^{-1} (figure 2a) are the stretching bands of O─H bonds in the kaol structure.
267 The band at 3697 cm^{-1} is assigned to surface O─H, in-phase stretching vibration. The bands
268 at 3666 and 3651 cm^{-1} are attributed to the surface O─H, out of phase stretching vibration
269 and the band at 3620 cm^{-1} is known as the inner O-H stretching vibration (Farmer, 1974;
270 Cases et al., 1982; Frost and Johansson, 1998; Frost et al., 2001; Balan, 2010; Mbey et al.,
271 2013). These bands are sensitive to cation substitution and planar defects. In the present case,
272 they are reasonably well defined, although less than what can be observed in well-ordered
273 kaol such as GB1 from the St. Austell deposit (Great Britain) (Cases et al., 1982, Balan et al.,
274 2010). Thus, the five samples display a relatively well-ordered structure, although partly

275 disordered by planar defects such as substitutions, or by intercalation of clay sheets of
276 different nature. The kaol silica Si─O stretching are observed at 1115 cm^{-1} and the symmetric
277 stretching of Si─O─Si appear at 1016 cm^{-1}. The aluminol bonds of the gibbsite clay sheet are
278 revealed through the bending vibration of Al─OH at 917 cm^{-1} and the ─OH (of Al─OH)
279 translational vibration at 786. The stretching bands of Si─O in quartz (free silica) are also
280 observable at 748 cm^{-1} and 694 cm^{-1} (Qtaitat et al., 2005; Al-Trawneh, 2005). The IR spectra
281 of the Na-kaol samples (not presented) exhibit the same characteristic bands.
282 TEM-EDX confirms the kaol-rich nature of all the samples (figure 3) as shown by the Si/Al
283 ratio from EDX which is close to 1 for all samples. Also the shape of the particles is clearly
284 hexagonal as expected for kaol, although less straightforward in MY3, where the particles are
285 significantly smaller than in the other samples, and form cluster aggregates.
286 The chemical analysis (table I) corresponds well to kaol minerals. In particular for the Kga2
287 sample, the data are comparable to that provided in the study by Mermut and Cano (2001).
288 Other elements (P_2O_5 and TiO_2) that are generally associated to kaol are also present. The
289 magnesium content, which could be due to traces of 2:1 clay minerals such as smectite, illite
290 or muscovite, is of interest (taking into account the detection limit of 0.02%) in MAC
291 (0.27%), MY3 (0.24%) and GZA4 (0.11%). Particle size analysis (table II), yielded for all
292 samples a D50 below 8 µm and a D90 below 25 µm. The value of D50 indicated relatively
293 high fine kaol fraction content in for all the samples. Using the chemical composition, the
294 structural formula of the kaol phase in each sample was approximated (table III). One should
295 note that, due to the impurities always associated to clay minerals, it is not possible to
296 accurately calculate the structural formulae, hence the proposed formulae are approximates.
297 The calculation procedure is based on the ideal hydroxyl composition and a total of 28
298 negative charges in the crystalline cell structure (Karathanasis, 2008). From the approximate
299 formulae, the presence of stoichiometric defaults are evidence. Coupling the structural

300 formula of the kaol in each sample and the elemental chemical composition, a mineralogical
301 quantification was done assuming the following: TiO_2 is a pure phase; K_2O is only due to
302 interlayer K in illite/muscovite. The results of the quantification (table IV) indicate that all the
303 samples have a kaol content higher than 80%. Illite content is especially significant in MY3
304 (10.4%) and GZA4 (4.8%).

305 ***3.2. Texture from Nitrogen adsorption/desorption isotherms***

306 The Nitrogen adsorption/desorption isotherms (figure 4) can be classified of type IV
307 according to the IUPAC recommendations (Sing et al., 1985). They exhibit a narrow
308 hysteresis between the adsorption and desorption branch, which is a usual feature for kaol,
309 assigned to beveled shaped mesopores (Sayed Hassan et al., 2005; Delineau, 1994).
310 The values of the BET specific surface area (SSA) (table V) indicate absence of significant
311 amount of micropores as suggested by the overall shape of the isotherms. Since the MgO
312 content is assumed here to be related to the presence of traces of swelling 2:1 clay, the SSA of
313 which is generally above 100 $m^2.g^{-1}$, one may expect an increase of the SSA with the MgO
314 content. This trend is indeed observed, except for the MAC sample. This exception is not a
315 contradiction, given that the difference may arise also from the crystalline disorder, the size,
316 the shape or the distortion within the clay platelets in each sample. The SSA of MAC also
317 agrees with the absence of swelling clay as previously mentioned from X-Ray analysis.

318 ***3.3. Surface energetic heterogeneity from DIS analysis of Argon adsorption isotherms.***

319 The experimental derivative adsorption isotherms (figure 5) display the feature usually
320 observed for phyllosilicates (Villiéras et al;, 1992; Bardot et al., 1998; Sayed Hassan et al.,
321 2005). A major peak is observed at medium adsorption energy (-6 to -1 Ln P/Po),
322 corresponding to the adsorption on basal faces. The broad shoulder at higher energy (< -6 Ln
323 P/Po) corresponds to the adsorption on edge faces. Using DIS, the isotherms were
324 successfully modelled with a sum of six to seven local derivatives (table VI). For all the

samples, the edge faces were modelled with domains 1 to 3, and the basal faces with domains 4 to 6 (table VI). Only MAC and MY3 fall out of this trend, since an additional basal domain (domain 7) was needed. As discussed in previous works (Sayed Hassan et al., 2005; Bardot et al., 1998), domains 1-2 are assigned to high energy adsorption sites of edge faces while domain 3 is characteristic of charged edge faces. The charge heterogeneity of the edge surface is evidenced by these three energy domains. The interactions of cations with basal faces is evidenced by domain 4 (average Ln P/P_0 = 4.3) and, from the work by Michot and Villiéras (2002) on synthetic saponite, it can be assumed that the cation density on these sites is less than 1 per 140 $\AA^2$. Domain 6 (average Ln P/P_0 = 2.4) is assigned to adsorption on basal low energy sites observed for all phyllosilicates. Domain 5 parameters are characteristic for the adsorbed cations and agree (as well as the parameters of domain 4 and 3) with the reported value for Na-kaol in a previous study (Sayed Hassan et al., 2005). The additional domain 7 (Ln P/P_0 = -4.6) for MAC and MY3 is probably due to the surface charge of associated sheets of smectite or illite-like clay mineral (Sayed Hassan et al., 2005). Given that the MgO contents of these two samples were the highest compared to the other three samples, smectite clay layers are the most likely to be considered.

The geometrical and structural information drawn from the measured basal and edge surface areas (BSA and ESA) are reported in table VII. The SSAs calculated from DIS are in the same order of magnitude as the classical N_2 BET SSA (average difference +1.3 m^2/g for the classical N_2 BET SSA). The fact that the N_2 BET SSAs are larger is often observed given that N_2 exhibits stronger interactions than Ar with adsorption sites (Bardot et al., 1998; Michot et Villiéras, 2002). As reported by Sayed Hassan et al. (2005), the basal surface area is not influenced by the nature of the cation and thus the cation density on this surface is probably low. Hence, one may assume that the difference in edge surface area is likely to be an

indication for the edge surface charge available for each sample, which should be supported by the titration results.

The thickness and diameter of particles are calculated using geometrical equations reported by Sayed Hassan et al. (2005). The edge surface area (ESA) and the basal surface (BSA) are used to compute, respectively, the length and the thickness. Although the coherent scattering domain and the thickness of the particles are different concepts, they can be identical in size for true nano-crystalline powder were each grain represent a coherent domain. That is why the grain size is usually larger than the coherent scattering domain. Comparing the calculated thickness values with the coherent scattering domain (D, in table VII) shows that the largest difference is 28 nm for the sample MY3, whereas it remains less that 10 nm for the other samples. From kinematical theory, this differences indicates that the crystallites are strain free for all the samples (Ungar et al., 2005). In addition, the fact that the size of the coherent domains follows the same trends as the particle size is a proof of the reliability of the DIS modeling. The lamellarity index which corresponds to the percentage of BSA, is lowest for the MY3 samples. The higher ESA observed for this sample may arise from two sources: (i) the illite contribution to ESA or (ii) the more anisotropic shape of this sample particles. If a contribution from illite is assumed, then the ESA of GZA4 would be expected to be the following higher value, but this is not the case. It is then believed that the kaolinite particles anisotropy could be a better cause. According to TEM observation, the anisotropy is higher for MY3 (figure 3) and this may be an a priori evidence for the previous assumption.

3.4. Electrokinetics.

Assuming that protonation-deprotonation on edge hydroxyls is the dominant origin of surface charge in kaol implies that, as for simple oxides, their electrophoretic mobility should depend on the pH and on the ionic-strength (lowest mobility at highest ionic strength), and the mobility curves should cross at a common point close to zero mobility. However, from the

374 results in figure 6 (left column for the raw kaol and right column for the corresponding Na-
375 kaol), only for PAH-Na a common intersection point may be fairly proposed, close to pH 4.
376 For the other samples, the observed trend is not consistent with the expected one, in particular
377 for the MAC, GZA4 and MY3 samples, for which the mobility curves are almost parallel to
378 the pH axis. Such a behavior is close to that observed for permanently charged clay minerals
379 such as smectites (Thomas et al., 1999). Indeed, a permanent charge originating from
380 isomorphic substitutions was evidenced from the calculated structural formula of all the
381 studied samples (see table IV). As reported by other authors (Tombácz and Szekeres, 2006),
382 the permanent charge dominates the electrokinetic behavior. In the case of MY3, GZA4 and
383 MAC, the more marked permanent charge behavior is consistent with the presence of
384 associated smectite layers as shown from the chemical analysis (table II) where significant
385 amounts of MgO and CaO (associated to exchangeable Calcium in smectites) were measured.
386 The domain 7 from DIS analysis (table VII) is in line with the proposed presence of few
387 smectite layers in MAC and MY3.

388 ***3.5. Charge on amphoteric surface sites.***

389 The surface excess values yielded by acid-base titration was normalized to the edge surface
390 area (ESA) obtained from DIS (figure 7). Although a clear separation between the protolytic
391 reactions at edge and basal sites and the ion exchange on permanent negative sites is not
392 strictly possible, normalization to ESA is still pertinent for comparison, since it is assumed
393 that protolytic edge reactions are well evidenced by titration. In the absence of permanent
394 charge, and by analogy with common (hydro)oxides, the titration curves are expected to
395 display dependence on the pH and on the ionic strength (highest surface excess at lowest ionic
396 strength), and a common intersection point indicating the Point of Zero Charge (PZC). Such
397 behavior was observed only for PAH-Na which exhibited a common intersection point at pH
398 close to 3.5 (figure 7e). The titration curves of the four other samples were shifted towards

399 higher pH according to decreasing ionic strength, as observed by Duc et al., (2006) and
400 modelled by Delhorme et al., (2010) for smectite and illite. An explanation for such
401 differences cannot be derived from the geometrical parameters (table VII) obtained using DIS
402 model, but rather from the structural differences between the samples. The permanent charge
403 electrostatically affects the dissociation of the edge sites by increasing the affinity for the
404 protons (Avena et al., 2003; Kraepiel et al., 1999; Delhorme et al., 2010), the amount of
405 titrated charge is likely to decrease with increasing permanent layer charge. The samples
406 MY3 (figure 7a), MAC (figure 7b) and GZA4 (figure 7c) have values for surface charge
407 ranging between 7 and 8 µmol/m^2 which may be of same range within experimental error and
408 indicative of significant permanent charge as also observed from their electrokinetic feature
409 (figure 6) which is similar to that of permanently charged minerals. Sample PAH with surface
410 excess from titration of 10 µmol/m^2 may be the least permanently charged as shown by its
411 mobility feature which depends on pH. The Kga2 sample is intermediate with a titration
412 charge of about 9 µmol/m^2. For all the samples, the values of surface excess range in a narrow
413 interval from 7 to 10µmol/m^2 and are associated to the kaol nature of the samples. The
414 difference amongst the samples may arise from the basal surface contribution which is
415 probably in line with the layer charge.
416 A low dependency of the titration curves to ionic strength is observed trough the slight split of
417 the curves upon ionic strength increase. This dependency is coherent with the existence of a
418 permanent negative charge as reported for 2:1 clay minerals (Duc et al., 2005b, 2006;
419 Tombácz and Szekeres, 2006). The point of zero salt effect (PZSE), which is reached as the
420 common intersection of the curves at different ionic strength, is only observed for the PAH
421 sample at pH~3.5. The trends of the curves for the other samples indicates a PZSE beyond pH
422 3. The point of zero net proton charge (PZNPC), which is the point at which the proton charge
423 goes to zero, is not unique, but rather ionic strength dependent, for all the samples. In

theoretical studies (Avena et al., 2003; Kraepiel et al., 1999), the absence of a PZNPC is shown to be due to the effect of the structural charge on dissociable edge sites. For ionic strength 0.01 M and 0.001 M, a common intersection for zero net proton charge exist for all the samples except for PAH within the pH interval (3.8 to 6.4). As reported by Chorover and Sposito (1995), because the PZNPC within our samples is ionic strength dependent (decreases to lower pH as the ionic strength increases) then this is an evidence for a permanent negative charge within these kaol. Because of the existence of this net permanent charge, no coincidence between the PZNPC and the PZSE is observed. This is also agreeing with the absence of PZC (in the studied pH range) (see figure 7) which is assumed to exist when PZNPC = PZSE (Sposito, 1989).

4. CONCLUSION

Examination of a broad set of properties on five kaol samples yields valuable information on the relationships between the crystal-chemical defects and the surface charge in electrolyte dispersion. The combination of these results allows the build-up of a consistent image of the morphological, structural, textural and surface properties of the studied kaol. Although most of the evidences are indirect and dispersed, some conclusions can be proposed:

- The permanent layer charge, resulting from non-negligible rates of substitution and stoichiometric defaults cause the titration curves to shift to lower pH with increasing ionic strength (MY3, MAC or GZA4 in particular); the proton consumption (due to pH-dependent, or variable charge) is influenced electrostatically by the layer charge which (even if low) and dominates the electrokinetic behavior;

- The DIS modeling was useful to probe presence of associated smectite-like minerals in samples MY3 and MAC. The presence of few 2:1 layers at the surface, after milling and dispersion of the sample, may affect the electrokinetic properties (MAC and MY3 samples);

- Modeling parameters derived from DIS are consistent with reported parameters for phyllosilicates. However, a clear link between the electrophoretic mobility and/or protolytic charge data and the geometrical parameters from DIS was not evidenced;

- In interfacial processes, the reactivity of kaol is controlled by its permanent charge. The negative electrophoretic mobility indicates that colloids stability will be controlled electrostatically by cations, hence given the low measured charges, delamination of kaol for particle size reduction may be useful to improve colloid stability.

The Cameroonian sample (MY3) is found to be a very fine kaol material with large specific surface area and high shape anisotropy, associated with significant layer charge. These factors may influence the particle orientation and particle-particle interaction in a composite material, depending on the charge feature of the associated compound.

A final remark can be that the purity of natural kaol can hardly be improved for analytical purposes because, unlike smectites, their particle size and shape prevent effective separation by centrifugation.

Acknowledgements

The first author is grateful to the French Ministry of Research and Higher Education for awarding a PhD grant. He acknowledges Odile Barrès, Renaud Gley, Lise Salsi, and Yves Waldvogel for training and technical assistance in FTIR, XRD and electrophoretic measurements.

Laurent Michot is acknowledged for fruitful remarks and discussions during the preparation of the manuscript.

471 **References**

472 Angove M.J., Johnson B.B. & Wells J.D. (1997) Adsorption of cadmium(II) on kaolinite.
473 *Colloids and Surfaces A: Physicochemical and Engineering Aspects*, **126**,137-147

474 Angove M.J., Johnson B.B. & Wells J.D. (1998) The Influence of Temperature on the
475 Adsorption of Cadmium (II) and Cobalt (II) on Kaolinite. *Journal of Colloid and Interface*
476 *Science,* **204**, 93–103.

477 Appel C., Ma L. Q. & Rhue R.D. (2003) Point of zero charge determination in soil and
478 minerals via traditional methods and detection of electroacoustic mobility. *Geoderma*, **113**,
479 77-93.

480 Avena, M.J., Mariscal, M.M. & De Pauli, C.P. (2003) Proton binding at clay surfaces in
481 water. *Applied Clay Science*, **24**, 3–9.

482 Balan E., Delattre S., Guillaumet M. & Salje E. K.H. (2010) Low-temperature infrared
483 spectroscopic study of OH-stretching modes in kaolinite and dickite. *American*
484 *Mineralogist,* **95**, 1257–1266.

485 Bardot F., Villiéras F., Michot L.J., François M., Gérard G. & Cases J.M. (1998) High
486 resolution gas adsorption study on illites permuted with various cations assessment of
487 surface energetic properties. *Journal of dispersion science and technology*, 19 (6-7), 739-
488 759.

489 Bergaya, F., Theng, B.K.G. & Lagaly, G. (2006) Clays in Industry. Pp 499-621 in: *Handbook*
490 *of Clay Science* (F.Bergaya, B.K.G. Theng, G. Lagaly, editors), Elsevier, Amtersdam.

491 Bolland M.D.A., Posner A.M. & Quirk J.P., (1980) PH-independent and pH-dependent
492 surface charges on kaolinite. *Clays and Clay Minerals*, **28**, 412-418.

493 Brady, P.V., Cygan, R.T. & Nagy, K.L. (1996) Molecular controls on kaolinite surface
494 charge. *Journal of Colloid Interface Science*, **183**, 356–364.

Cases J.M., Lietard O, Yvon J. & Delon J.F. (1982) Etude des propriétés cristallochimiques, morphologiques, superficielles de kaolinites désordonnées. *Bulletin de Mineralogie,* 105, 439-455.

Cases J.M., Villiéras F. & Michot L.J., (2000) Les phénomènes d'adsorption, d'échange ou de rétension à l'interface solide-solution aqueuse. *C.R. Acad. Sci. Paris, Sciences de la terre et des planets*, 763-773.

Chassagne C., Mietta F. & Winterwerp J.C. (2009). Electrokinetic study of kaolinite suspensions. *Journal of colloid and interface science*, **336**, 352-359.

Chorover J. and Sposito G. (1995) Surface charge characteristics of kaolinitics tropical soils. *Geochimica et Cosmochimica Acta*, **59**, 875-884.

Delhorme M., Labbez C., Caillet C. & Thomas F. (2010) Modelling acid-base properties of 2:1 clays. The role of electrostatics. *Langmuir,* **26**, 240-9249.

Delineau T. (1994) *Les argyles kaoliniques du bassin de charentes (France): Analyses typologiques, cristallochimique, speciation du fer et applications*. Thèse de Dotorat, INPL-Nancy (France), 627p.

Dubreuilh J., Marchadour P. & Thiry M., (1984) Cadre geologique et mineralogy des argiles des charentes, France. *Clay Minerals*, **19**, 29-41.

Duc M., Thomas F. & Gaboriaud F. (2005a) Sensitivity of the acid-base properties of clays to the methods of preparation and measurement 1. Literature review. *Journal of Colloid and Interface Science*, **289**, 139-147.

Duc M., Thomas F. & Gaboriaud F. (2005b) Sensitivity of the acid-base properties of clays to the methods of preparation and measurement 2. Evidence from continuous potentiometric titrations. *Journal of Colloid and Interface Science*, **289**, 148-156.

518 Duc M., Thomas F. & Gaboriaud F., (2006) Coupled chemical processes at clay/electrolyte
519 interface: A batch titration study of Na-montmorillonites. *Journal of Colloid and Interface*
520 *Science*, **300**, 616-625.
521 Farmer V.C., (1974). The layer silicates in: *The Infrared spectra of minerals* (Farmer VC,
522 editor). London: Mineralogical Society, 331-363.
523 Frost R. & Johansson U. (1998) Combination of bands in the infrared spectroscopy of kaolins.
524 A DRIFT spectroscopic study. *Clays and Clay Minerals,* **46**, 466-477.
525 Frost R.L., Makó É., Kristóf J., Horváth E. & Kloprogge J.T. (2001) Modification of kaolinite
526 surfaces by mechanochemical treatment. *Langmuir*, **17**, 4731–4738.
527 Gupta V. & Miller J. D. (2010) Surface force measurements at the basal planes of ordered
528 kaolinite particles. *Journal of Colloid and Interface Science*, **344**, 362-371.
529 Herrington T.M., Clarke A.Q. & Watts J.C. (1992) The surface charge of kaolin. *Colloids and*
530 *surfaces*, **68**, 161-169.
531 Hong H., Cheng F. Yin K. Churchman G. J. and Wang C. (2015). Three-component mixed-
532 layer illite-smectite-kaolinite (I/S/K) minerals in hydromorphic soils, south China. *American*
533 *Mineralogist*, 100 (8-9), 1883-1891.
534 Huertas F.J., Chou L. & Wollast R. (1998) Mechanism of kaolinite dissolution at room
535 temperature and pressure: Part1. Surface speciation. *Geochimica et Cosmochimica acta*, **62**,
536 417-431.
537 Ikhsan J., Johnson B.B. & Wells J.D. (1999) A Comparative study of the adsorption of
538 transition metals on kaolinite. *Journal of Colloid and Interface Science*, **217**, 403-410.
539 Karathanasis A.D. (2008) Structural allocation of clay mineral elemental components. Pp
540 465-483 in *Methods of Soil analysis. Part 5. Mineralogical methods* (A. L. Ulery & L. R.
541 Drees editors), SSSA Book Series N^{o} 5, USA.

Kraepiel, A.M.L., Keller, K. & Morel, F.M.M. (1998) On the acid–base chemistry of permanently charged minerals. *Environmental Science and Technology*, **32**, 2829–2838.

Kraepiel A.M.L., Keller K., & Morel F.M.M. (1999) A Model for Metal Adsorption on Montmorillonite. *Journal of Colloid and Interface Science*, **210**, 43-54.

Kosmulski M. & Dahlsten P. (2006) High ionic strength electrokinetics of clay minerals. *Journal of Colloid and Interface Science*, **291**, 212-218.

Ma C. & Eggleton R.A. (1999a) Cation exchange capacity of kaolinite. *Clays and Clay Minerals,* **47**, 181-191.

Ma C. & Eggleton R.A (1999b) Surface layer type of kaolinite: A high-resolution transmission electron microscope study. *Clays and Clay Minerals,* **47**, 181-191.

Mbey J.A., Thomas F., Ngally Sabouang C.J., Liboum & Njopwouo D. (2013) An insight on the weakening of the interlayer bonds in a Cameroonian kaolinite through DMSO intercalation. *Applied Clay Science,* 83-84, 327–335.

Mbey J. A., Hoppe S. & Thomas F. (2015) Cassava starch-kaolinite composite films. Thermal and mechanical properties related to filler-matrix interactions. *Polymer Composites*, **36**, 184-191.

Mbey J. A. & Thomas F. (2015) Components interactions controlling starch-kaolinite composite films properties. *Carbohydrate Polymers*, **117**, 739-745.

Mbey J. A., Hoppe S. & Thomas F. (2012) Cassava starch-kaolinite composite film. Effect of clay content and clay modification on film properties. *Carbohydrate Polymers*, **88**, 213-22.

Menezes R.A., Paz S.P.A., Angélica R.S.A., Neves R.F., Neumann R., Faulstich F.R.L. & Pergher S.B.C. (2017) Synthesis of ultramarine pigments from Na-A zeolite derived from kaolin waste from the Amazon. *Clay Minerals*, **52**, 83 – 95.

Mermut A.R. and Cano A. G. (2001) Baseline studies of the clay minerals society source clays: chemical analyses of major elements. *Clays and Clay Minerals*, **49**(5), 381–386.

567 Michot L.J. & Villiéras F. (2002) Assessment of surface energetic heterogeneity of synthetic
568 Na-saponites. The role of layer charge. *Clay Minerals*, **37**, 39-57.
569 Moll W.F. Jr. (2001) Baseline studies of the clay minerals society source clays: geological
570 origin. *Clays and Clay minerals*, **49**, 374-380.
571 Murray H. H., (1988) Kaolin Minerals: their genesis and occurrences. Pp. 67-89 in *Hydrous*
572 *Phyllosilicates* (S.W. Bailey, editor), Mineralogical Society of America.
573 Njoya A., Nkoumbou C., Grosbois C., Njopwouo D., Njoya D., Courtin-Nomade A., Yvon J.,
574 and Martin F. (2006). Genesis of Mayouom kaolin deposit (western Cameroon). *Applied*
575 *Clay Science*, 32, 125-140.
576 Qtaitat M.A. & Al-Trawneh I.N. (2005) Characterization of kaolinite of the Baten El-Ghoul
577 region/south Jordan by infrared spectroscopy. *Spectrochimica Acta Part A: Molecular and*
578 *Biomolecular Spectroscopy*, **61**, 1519–1523.
579 Rowlands W.N. & O'brien R.W. (1995) The Dynamic Mobility and Dielectric Response of
580 Kaolinite Particles. *Journal of Colloid and Interface Science*, **175**, 190-200.
581 Sakharov B. A., Lindgreen H., Salyn A. L., and Drits V. A., (1999) Mixed-layer kaolinite-
582 illite-vermiculite in North Sea shales. *Clay minerals*, **34**, 333-344.
583 Sayed Hassan M., Villiéras F., Razafitianamaharavo A. & Michot L.J. (2005) Role of
584 exchangeable cations on geometrical and energetic surface heterogeneity of kaolinites.
585 *Langmuir*, **21**, 12283-12289.
586 Schofield R. K. & Samson H. R. (1954) Flocculation of kaolinite due to the attraction of
587 oppositely charged crystal faces. *Discussion of the Faraday Society*, **18**, 135-145.
588 Schroeder P.A. & Shiflet J. (2000) Ti-bearing phases in the Huber formation, an east gorgia
589 kaolin deposit. *Clays and Clay minerals*, **48**, 151-158.
590 Schroth B.K. & Sposito B. (1997) Surface charge properties of kaolinite. *Clays and Clay*
591 *mineral*, **45**, 85-91.

592 Sing K.S.W., Everett D.H., Haul R.A.W., Moscou L., Pierotti R.A., Rouquérol J. &
593 Siemieniewska T. (1985) Reporting physisorption data for gas/solid systems with special
594 reference to the determination of surface area and porosity. *Pure and Applied Chemistry*, **57**,
595 603-619.
596 Sposito G. (1989) Surface reaction in natural aqueous colloidal system. *Chimica*, **43**, 169-176.
597 Tertre E., Castet S., Berger G., Loubet M. & Giffaut E. (2006) Surface chemistry of kaolinite
598 and Na-montmorillonite in aqueous electrolyte solution at 25 and 60°C: Experimental and
599 modelling study. *Geochimica et Cosmochimica acta*, **70**, 4579-4599.
600 Thomas F., Michot L.J., Vantelon D., Montargès E., Prélot B., Cruchaudet M. & Delon J.F.
601 (1999) Layer charge and electrophoretic mobility of smectites. *Colloids and Surfaces*, **159**,
602 351-358.
603 Thomas F., Prélot B., Villiéras F. & Cases J.M. (2002) Electrochemical properties at the
604 aqueous-solid interface and heterogeneity of surface. *C.R. Geoscience*, **334**, 633-648.
605 Tombácz E. & Szekeres M. (2006). Surface charge heterogeneity of kaolinite in aqueous
606 suspension in comparison with montmorillonite. *Applied Clay Science*, **34**, 105-124.
607 Ungár, T., Tichy, G., Gubicza, J. and Hellmig, R. J. (2005). Correlation between subgrains
608 and coherently scattering domains. *Powder Diffraction*, *20*(4), 366-375. DOI:
609 10.1154/1.2135313
610 Villieras F., Case J.M., François M., Michot L.J. & Thomas F. (1992) Texture and surface
611 energetic heterogeneity of solids from modelling of low pressure gas adsorption isotherms.
612 *Langmuir*, **8**, 1789-1795.

Villieras F., Michot L.J., Bardot F., Cases J.M., François M., and Rudzinski W., (1997). An improved derivative isotherm summation method to study surface heterogeneity of clay minerals. *Langmuir*, **13**, 1104-1117.

Villieras F., Michot L.J., Bardot F., Chamerois M., Eypert-Blaison C., François M., Gérard G. and Cases J.M., (2002). Surface heterogeneity of minerals. *C.R. Geoscience*, **334**, 597-609.

Williams D. J. A. & Williams K. P., (1978) Electrophoresis and zeta potential of kaolinite. *Journal of Colloid and Interface science*, **65**, 79-87.

Zhou Z. & Gunter W.D. (1992) The nature of the surface charge of kaolinite. *Clays and Clay Minerals*, **40**, 365-368.

Zhu X., Zhu Z., Lei X., Yan C. (2016) Defects in structure as the sources of the surface charges of kaolinite, Applied Clay Science, **124–125**, 127–136.

Graphical Abstract

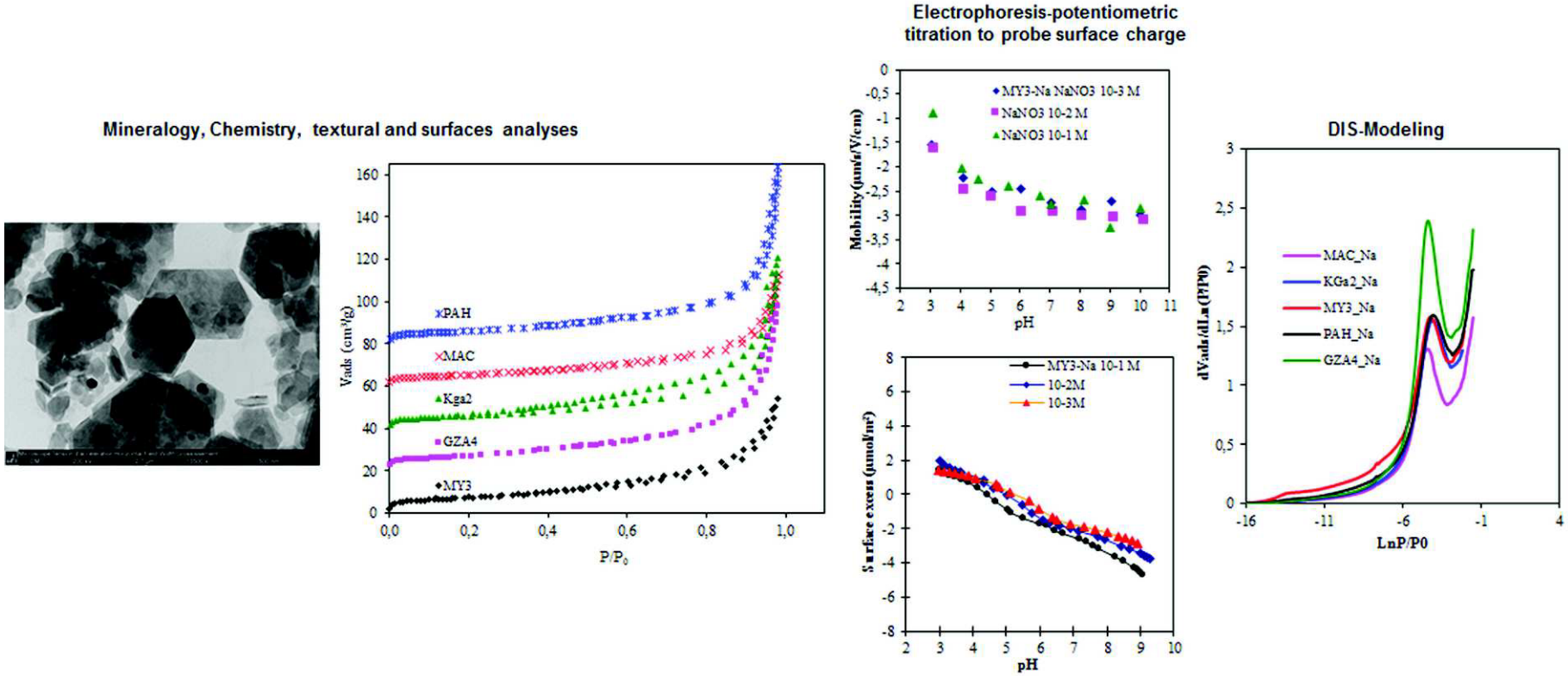

Analysis of the crystallo-chemical, textural and surface properties at solid-gas and solid-electrolyte interface of five kaolinites

*Highlights (for review)

Surface properties of five natural kaolinite samples are analyzed > Deviation from stoichiometric defaults and some substitutions are evidenced from chemical analyses > The permanent charge electrostatically influence the proton consumption during acid-base titration > Electrokinetic behavior is dominate by the permanent charge > From the DIS modeling the presence of trace 2:1 clay layer on some samples was probe.

Table 2

Click here to download Table: Table 2.docx

Table II: Size distribution of the kaol samples

Samples	**MY3**	**Kga2**	**GZA4**	**MAC**	**PAH**
D10	1.6	1.6	0.94	1.04	1.17
D50	7.22	7.19	2.76	3.64	5.66
D90	23.9	21.16	7.11	15.67	21.03
Mode	10.4	9.6	3.6	6.25	8.77

Table III: Structural formulae of the studied kaolinites, calculated from chemical analysis

	Average structural formula
MY3	$(Al_{1.94}\ Fe_{0.06})(Si_{1.98}\ Fe_{0.02})O_5(OH)_4Ca_{0.002}\ Mg_{0.02}$
MAC	$(Al_{1.94}Si_{0.02}Fe_{0.01}Mg_{0.02}Ca_{0.01})(Si_2O_5)(OH)_4$
PAH	$(Al_{1.98}Fe_{0.02})(Si_{1.98}\ Fe_{0.02})O_5(OH)_4$
Kga2	$(Al_{1.98}Fe_{0.02})(Si_{1.99}\ Fe_{0.01})O_5(OH)_4\ (Fe_{0.01})$
GZA4	$(Al_{1.95}Fe_{0.04}Ca_{0.01})(Si_{1.99}\ Mg_{0.01})O_5(OH)_4$

Table 4

Click here to download Table: Table 4.docx

Table IV: Mineralogical composition of the kaolinite samples

	Kaolinite	**Illite/Muscovite**	**TiO_2**	**SiO_2**	**Iron Oxide**	**Total**
MY3	83.3	10.4	3.4	0.0	0.0	97.1
MAC	95.8	0.2	1.5	0.1	0.1	97.7
PAH	94.9	1.3	2.2	0.5	0.0	98.8
Kga2	95.4	0.3	2.2	0.5	0.3	98.7
GZA4	92.4	4.8	1.2	0.5	0.1	99.0

Table 5

Click here to download Table: Table 5.docx

Table V: Specific Surface Area (±1 m^2/g) and CEC of the kaol samples

	CBET	Vm BET cm^3/g	S BET m^2/g	CEC meq/100g
MY3	130	5.9	25.9	6
GZA4	79	5.7	24.9	4.1
Kga2	88	4.8	21.0	10.6
MAC	100	4.3	18.7	7.9
PAH	100	5.0	22.0	4

Vm : monolayer volume from BET modeling; CBET: BET constant

Table 6
Click here to download Table: Table 6.docx

Table VI: Main parameters derived from the application of the DIS method to argon adsorption at 77 K on Na-exchanged kaolinites.

		MY3	**MAC**	**Kga2**	**GZA4**	**PAH**
Domain 1	$\ln(P/P_0)$	-13.3	-12.6	-12.7	-12.0	-13.1
	V_m	0.16	0.06	0.04	0.06	0.10
	w/kt	1.2	0.4	0.0	0.0	0.0
Domain 2	$\ln(P/P_0)$	-10.3	-10.3	-10.5	-10.6	-10.5
	V_m	0.52	0.11	0.13	0.11	0.18
	w/kt	-0.7	0.2	0.0	0.0	0.0
Domain 3	$\ln(P/P_0)$	-6.9	-7.0	-6.8	-6.9	-6.9
	V_m	1.10	0.47	0.60	0.68	0.82
		-0.2	-0.10	-0.8	-0.8	-0.8
Domain 4	$\ln(P/P_0)$	-4.2	-4.2	-4.3	-4.4	-4.3
	V_m	1.87	0.69	2.58	3.65	2.54
	w/kt	1.5	1.8	1.5	2	1.5
Domain 5	$\ln(P/P_0)$	-3.6	-3.6	-3.6	-3.5	-3.6
	V_m	0.35	0.07	0.76	1.24	0.85
	w/kt	1.5	1.8	1.5	1.5	1.5
Domain 6	$\ln(P/P_0)$	-2.4	-2.4	-2.4	-2.3	-2.4
	V_m	1.29	1.29	1.24	1.21	1.39
	w/kt	0.0	0.0	0.0	0.0	0.0
Domain 7	$\ln(P/P_0)$	-4.5	-4.6			
	V_m	1.07	1.77			
	w/kt	1.5	1.8			

Table 7
Click here to download Table: Table 7.docx

Table VII: Geometrical and structural parameters deducted from application of DIS to Argon adsorption at 77 K on Na-kaolinites. The thickness obtained by the Scherrer equation from X-ray diffraction of the powder is given for comparison.

	MY3	MAC	KGa2	GZA4	PAH
ESA (m^2/g)	6.6	2.4	2.9	3.1	4.1
BSA (m^2/g)	17.0	14.2	17.0	22.6	17.8
SSA (m^2/g)	23.6	16.6	19.9	25.7	21.9
Length (nm)	267	735	608	569	430
D (XRD, Scherrer)* (nm)	17	44	34	26	34
Thickness (nm)	45	54	45	34	43
Lamellarity Index (%)	72	86	88	88	81

* *D* is the Scattering Coherent Domain calculated from X-ray pattern using the full width at maximum half-height of the d_{001} diffraction peak and the Scherrer equation.

Table 1

Table I: Sources and chemical composition (percentages of oxides of the major elements) of the kaolinite samples

Samples	**MY3**	**GZA4**	**Kga2**	**MAC**	**PAH**
Sources	Cameroon (Mayouom) Njoya et al., 2006	France (Charentes) Dubreuilh et al., 1984	USA (Georgia) Moll, 2001	USA (Macon, Georgia) Schroeder and Shiflet, 2000	USA (Georgia) Schroeder and Shiflet, 2000
Chemical Composition					
SiO_2	44.28	45.47	43.89	45.20	44.33
Al_2O_3	34.21	36.66	37.37	36.65	37.34
Fe_2O_3	1.97	1.27	1.17	0.44	1.13
MnO	0.01	0.00	0.00	0.00	0.00
MgO	0.24	0.11	0.03	0.27	0.05
CaO	0.04	0.18	< L.D	0.26	< L.D
Na_2O	< L.D	0.04	< L.D	< L.D	< L.D
K_2O	1.23	0.57	0.04	0.02	0.15
TiO_2	3.39	1.21	2.17	1.50	2.18
P_2O_5	0.26	0.06	0.05	< L.D	0.05
LOI	13.70	14.01	14.29	14.67	14.40
Total	99.33	99.59	99.01	99.01	99.63

L.D: detection limit; LOI: loss on ignition

Figure 1

Click here to download Figure: Figure 1_DRX.docx

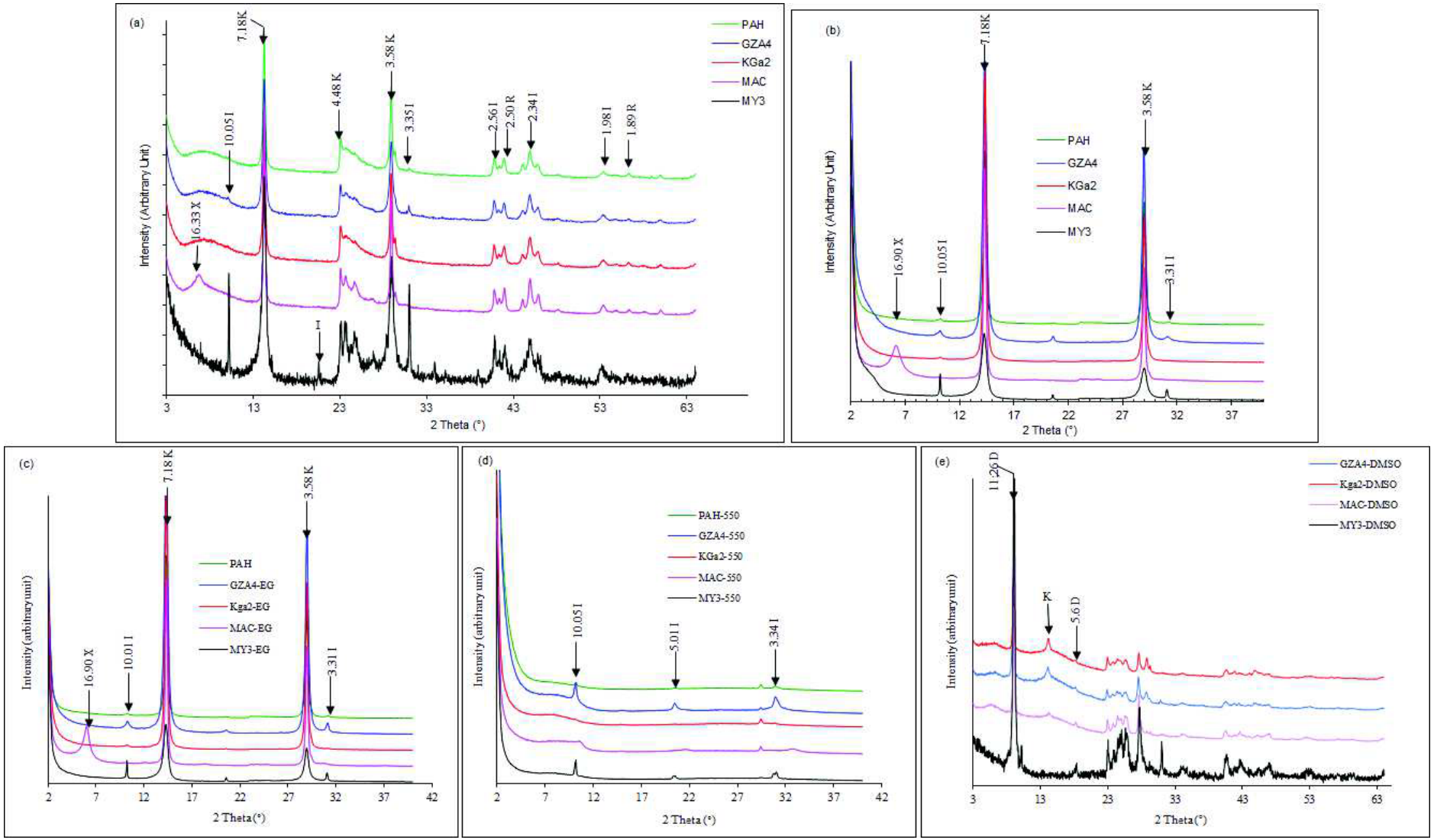

Figure 1: DRX pattern of the raw kaolinite samples: (a) bulk sample (< 40 µm) (b) oriented samples (< 2 µm) (c) Ethylene glycol solvated samples (d) Heated samples at 550 °C (e) DMSO intercalated samples

K: Kaolinite; I: Illite; R: titanium oxide (rutile); D: kaolinite-DMSO intercalated; X: interstratification

Figure 2
Click here to download Figure: Figure 2.docx

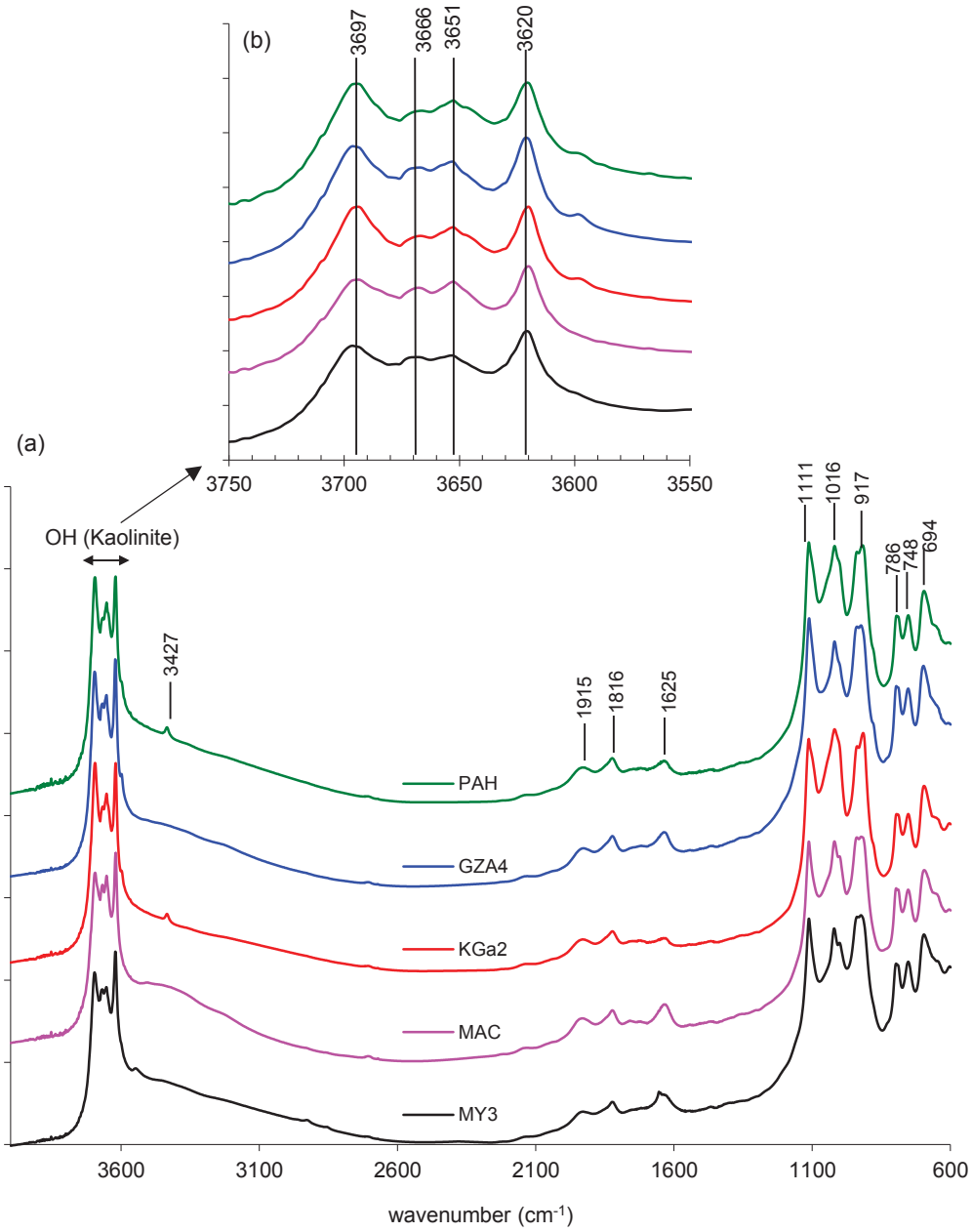

Figure 2: FTIR spectra of the kaolinite samples (a) the entire spectra (b) zooming in the OH elongation vibration domain.

Figure 3
Click here to download Figure: Figure 3.docx

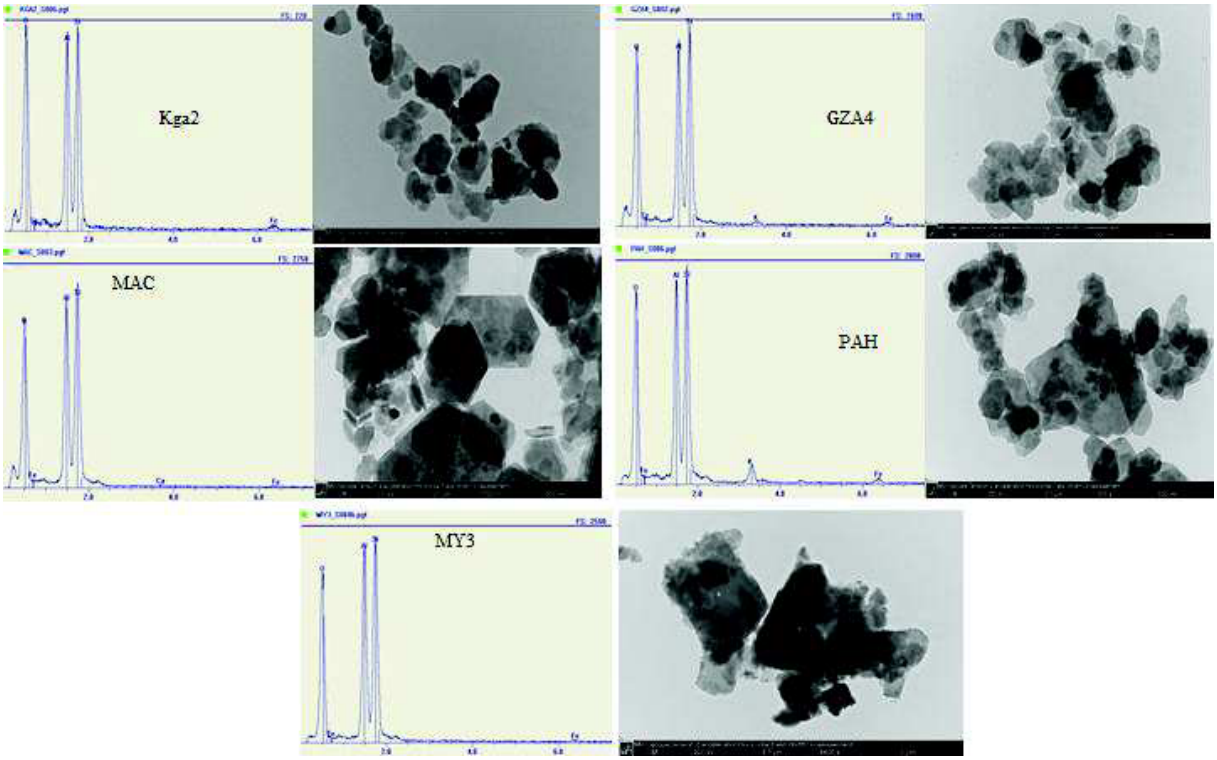

Fig. 3: TEM-EDX showing and Si/Al ratio of almost 1 for all the samples.

Figure 4
Click here to download Figure: Figure 4.docx

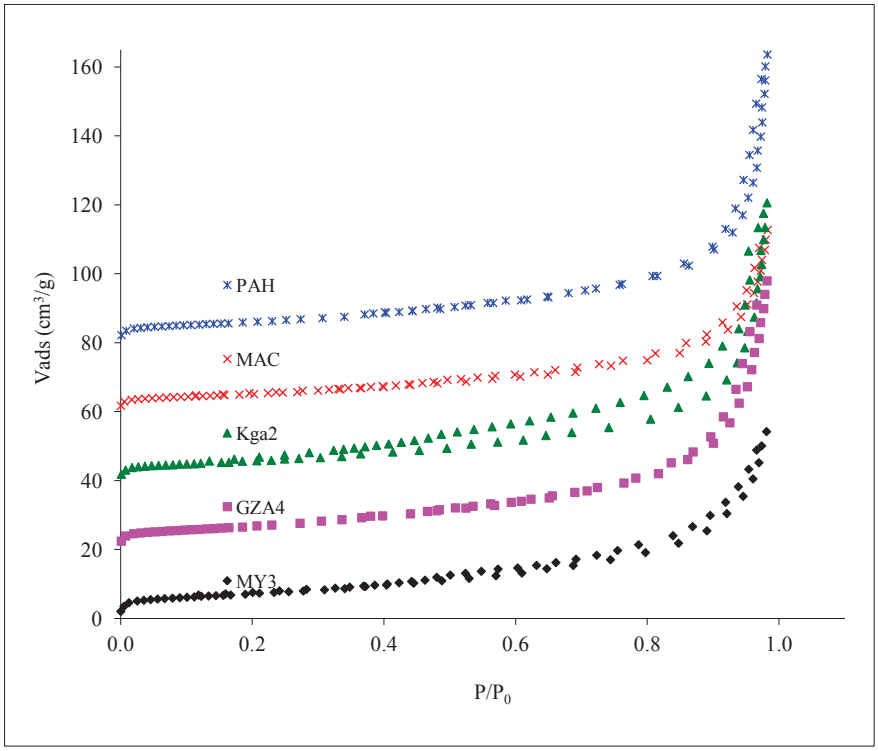

Curves shifted of 20 cm^3/g

Fig. 4: N_2 Adsorption isotherms at 77 K on the kaolinite samples

Figure 5
Click here to download Figure: Figure 5.docx

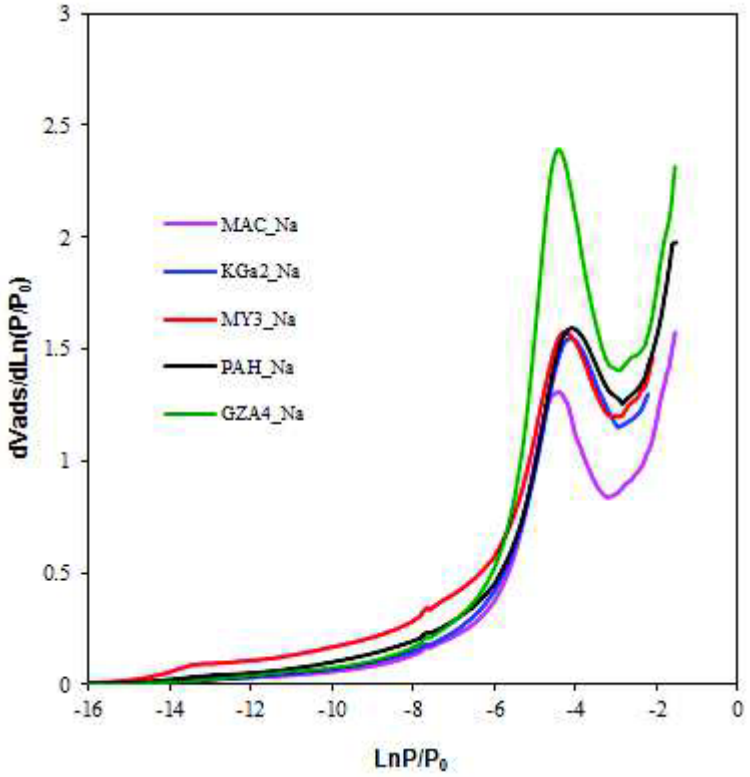

Fig. 5: Experimental derivative argon adsorption isotherms at 77 K of the Na-kaolinites

Figure 6

Click here to download Figure: Figure 6.docx

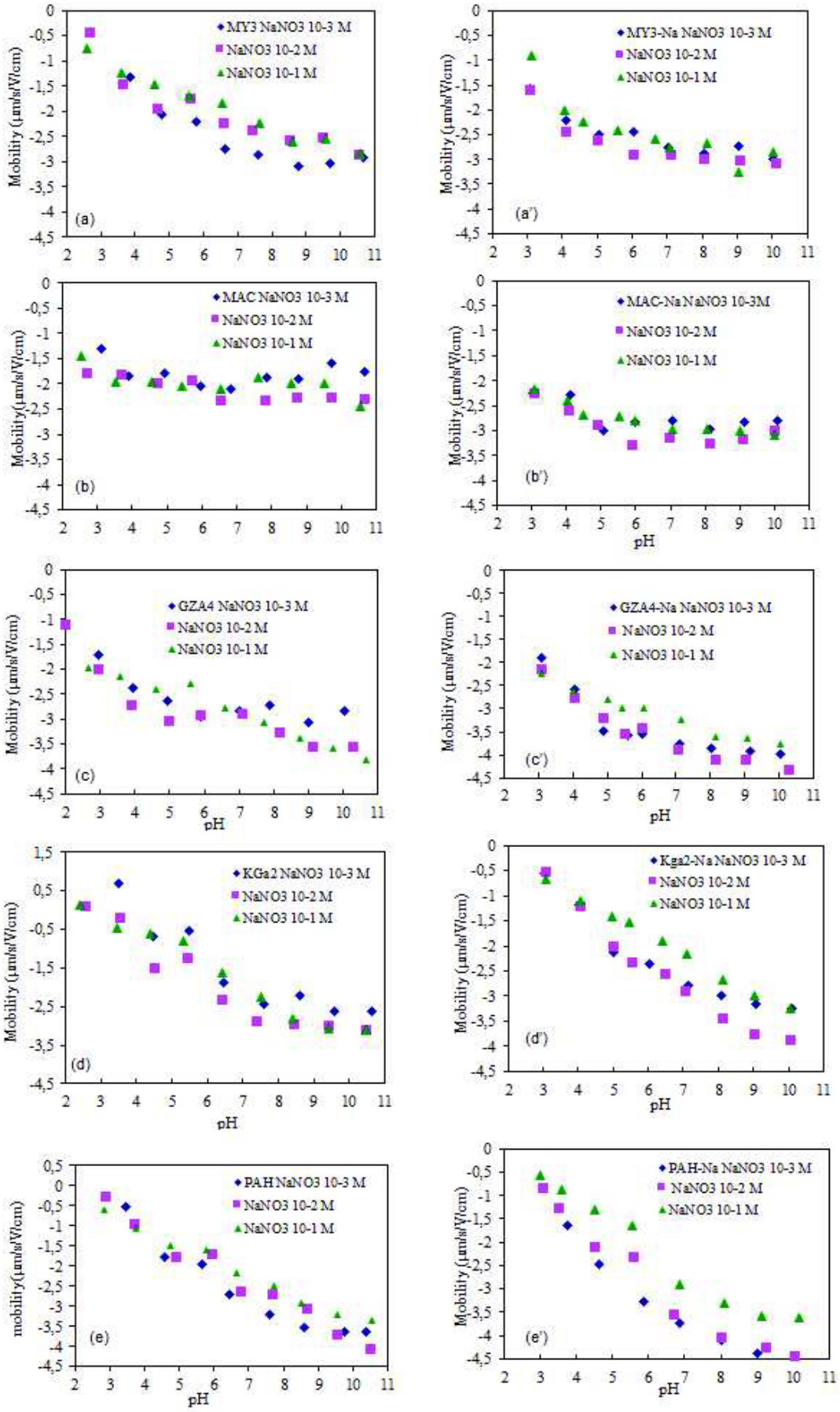

Fig. 6: Electrophoretic mobility versus pH on raw (left) and Na-Kaolinite (right) in $NaNO_3$ background

Figure 7
Click here to download Figure: Figure 7.docx

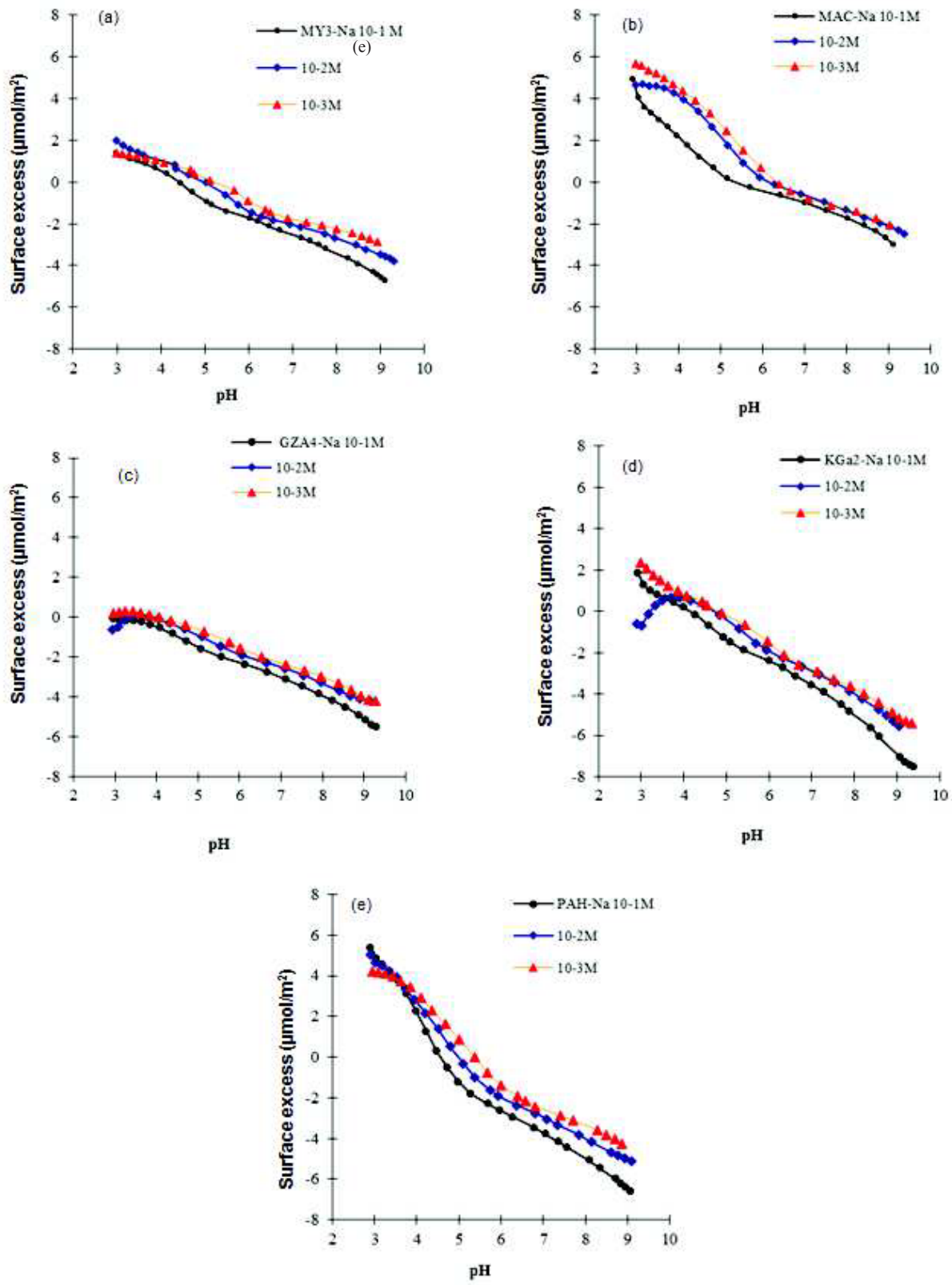

Figure 7: Apparent surface charge of the Na-exchanged kaolinite samples in $NaNO_3$ background, normalised to the edge surface area obtained from DIS modeling